ACS APPLIED MATERIALS & INTERFACES

www.acsami.org

Research Article

Unveiling the Electrocatalytic Activity of 1T′-$MoSe_2$ on Lithium-Polysulfide Conversion Reactions

Kiran Mahankali,[§] Sundeep Varma Gottumukkala,[§] Nirul Masurkar, Naresh Kumar Thangavel,* Rahul Jayan, Abdulrazzag Sawas, Sudhan Nagarajan, Md Mahbubul Islam,* and Leela Mohana Reddy Arava*

Cite This: *ACS Appl. Mater. Interfaces* 2022, 14, 24486–24496

Read Online

ACCESS | Metrics & More | Article Recommendations | Supporting Information

ABSTRACT: The dissolution of intermediate lithium polysulfides (LiPS) into an electrolyte and their shuttling between the electrodes have been the primary bottlenecks for the commercialization of high-energy density lithium−sulfur (Li−S) batteries. While several two-dimensional (2D) materials have been deployed in recent years to mitigate these issues, their activity is strictly restricted to their edge-plane-based active sites. Herein, for the first time, we have explored a phase transformation phenomenon in a 2D material to enhance the number of active sites and electrocatalytic activity toward LiPS redox reactions. Detailed theoretical calculations demonstrate that phase transformation from the 2H to 1T′ phase in a $MoSe_2$ material activates the basal planes that allow for LiPS adsorption. The corresponding transformation mechanism and LiPS adsorption capabilities of the as-formed 1T′-$MoSe_2$ were elucidated experimentally using microscopic and spectroscopic techniques. Further, the electrochemical evaluation of phase-transformed $MoSe_2$ revealed its strong electrocatalytic activity toward LiPS reduction and their oxidation reactions. The 1T′-$MoSe_2$-based cathode hosts for sulfur later provide a superior cycling performance of over 250 cycles with a capacity loss of only 0.15% per cycle along with an excellent Coulombic efficiency of 99.6%.

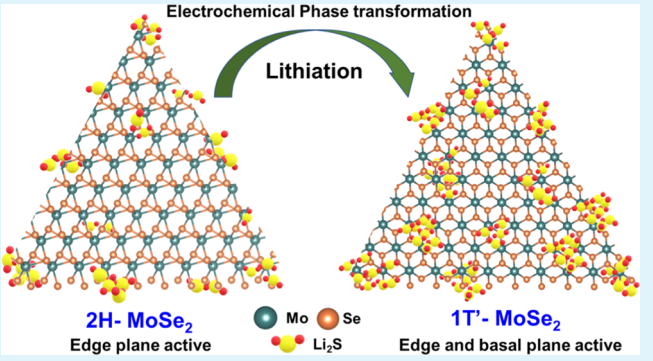

KEYWORDS: *lithium−sulfur, 2D material, transition metal dichalcogenide, phase transformation, electrocatalysis*

1. INTRODUCTION

Lithium−sulfur (Li−S) redox chemistry has turned into one of the most exciting energy storage technologies because of its high theoretical capacity (1673 mAh/g) and energy density (2600 Wh/kg), which is ∼10 times higher than any of the contemporary Li-ion batteries.[1,2] However, the Li−S cell performance often deteriorates due to several issues including rapid capacity fade, limited cycle life, and reduced Coulombic efficiency, obstructing their commercialization. Among various reasons underpinning such performance barriers, the diffusion of intermediate lithium polysulfides (LiPS) into the electrolyte and their subsequent shuttling between the electrodes are of prime concern. While past efforts have focused on exploring carbonaceous host materials, their inherent nonpolar nature only allows for weak interaction with the polar LiPS making the shuttling effect inevitable upon extended cycling.[1,3] To further alleviate the shuttle-related issues, researchers have proposed several strategies such as anchoring the LiPS within polar cathode surfaces, which restricts the polysulfide dissolution and provides an excellent Coulombic efficiency along with cycle life.[4,5] Therefore, exploring the design principle of anchoring LiPS physically and chemically via employing a polar substrate is highly appealing.[6,7] Along these lines, the use of electrocatalysts in the multistep sulfur redox process has shown enormous potential in the trapping of polysulfides, enhancing the specific capacity along with cycle life and showing excellent reversibility.[8]

While traditional electrocatalysts such as platinum-based materials remarkably improve the Li−S performance, their high cost and scarce resources persuade researchers to explore alternative catalysts for energy applications.[9−11] In this context, transition metal dichalcogenides (TMDs) have attracted much interest to accelerate the Li−S reaction kinetics and their overall performance.[10,12−14] Through systematic electrochemical evaluation, several researchers have demonstrated the importance of such electrocatalyst nanoparticles on LiPS

Received: March 29, 2022
Accepted: May 4, 2022
Published: May 18, 2022

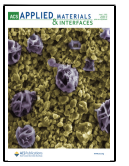

multistep conversion reactions.[15,16] It has been previously demonstrated that highly catalytic edge planes can effectively adsorb LiPS and favor the deposition and oxidation of the discharge end products.[11,17−19] It is well agreed upon that the exceptional catalytic activity of TMDs arises from the versatile and tunable electronic structure of transition metal d-orbitals and undercoordinated surface atoms, the so-called edge planes.[20,21] On one hand, several strategies have been explored to enhance the number of edge planes in TMDs to improve their activity. However, given that the inherently inert basal plane is considerably more stable and highly exposed compared to the edge planes, it would be rational to activate it to further enhance both the overall number of active sites and electrocatalytic properties. In this regard, researchers have vigorously explored strategies including plasma or electron beam irradiation, defect engineering, chemical activation, doping, and so on.[22−25] On the other hand, a phase change of TMDs from 2H to 1T′ by excess lithium intercalation was found to dramatically activate the basal planes and enhance the catalytic activity of the materials.[26−30] More importantly, previous studies suggest that such phase engineering of TMDs is strongly influenced by the energy difference between the two phases, giving the researchers the ability to precisely identify and tailor the materials.[31,32] While such phase transformations and associated catalytic activities were reported in the case of traditional water-splitting reactions and lithium-ion batteries, they were never reported in Li−S redox reactions.[33]

Hence, we have chosen to study the highly advantageous phase transformations for Li−S redox chemistry and monitor the basal plane's activity by exploring $MoSe_2$ as a model TMD electrocatalyst. Herein, the energy difference (ΔE) between the 2H and 1T′ structures of $MoSe_2$ was found to be substantially smaller (0.33 eV) compared to WS_2 (0.54 eV) or MoS_2 (0.55eV), making $MoSe_2$ an ideal candidate for phase engineering.[34] Besides, most of the experimental and computational studies show that $MoSe_2$ is more catalytic than other TMDs like MoS_2.[35−37] Even in Li−S batteries, $MoSe_2$ was previously used in conjunction with a carbonaceous host and demonstrated to provide anchoring sites for LiPS and an excellent electrocatalytic activity toward LiPS conversion.[38−40] In this study, we performed density functional theory (DFT) simulations to probe the LiPS adsorption behavior on the basal plane and edge sites of the metallic 1T′-$MoSe_2$. Interestingly, our computational study indicated that the reconstructed 1T′ phase from the 2H phase due to lithium intercalation exhibits significantly higher LiPS adsorption strengths on both the basal plane and edge sites compared to 2H-$MoSe_2$. Furthermore, ex situ scanning electron microscopy (SEM) and X-ray photoelectron spectroscopy (XPS) studies were employed to corroborate the DFT-predicted phase transformation in $MoSe_2$, their influence on LiPS anchoring sites, and associated mechanisms. The electrocatalytic activity of phase-transformed $MoSe_2$ (henceforth referred to as 1T′-$MoSe_2$) on Li−S redox reactions was studied using typical electrochemical characterization and cycling performance by galvanostatic charge−discharge studies.

2. RESULTS AND DISCUSSION

2.1. LiPS Adsorption Behavior on Different Phases of $MoSe_2$. Understanding the effect of atomic sites on the crystal surface is pivotal to controlling electrocatalytic chemical reactions. However, only limited efforts have been dedicated to understanding the behavior of different sites on TMDs toward LiPS conversion in Li−S batteries and their subsequent employment as electrocatalysts. Typically, bulk $MoSe_2$ comprising sandwiched Se−Mo−Se monolayers bonded together by weak van der Waal interactions exhibits two phases, 2H and 1T′.[41] Herein, we perform DFT calculations to understand the adsorption capabilities of the S_8 and LiPS species on different phases and sites of $MoSe_2$ substrates in relation to the suppression of the shuttle effect. The details of the computational methods are provided in the Supporting Information (SI). The binding energy values were obtained using the formula $E_{ads} = E_{Li_2S_n} + E_{AM} - E_{Li_2S_n + AM}$, where $E_{Li_2S_n}$, E_{AM}, and $E_{Li_2S_n + AM}$ denote the total energies of isolated polysulfides, anchoring material (AM), and the polysulfides adsorbed system, respectively. As expected, the basal planes of 2H-$MoSe_2$ (Figures 1 and S1) demonstrated the lowest

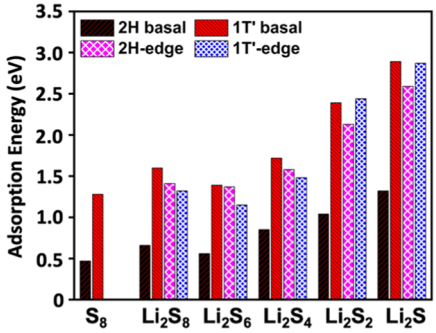

Figure 1. Adsorption energies of S_8 and Li_2S_n on the basal plane and edge sites of 2H and 1T′-$MoSe_2$.

binding capabilities toward most liquid LiPS and solid charge−discharge end products (like Li_2S or S_8) and are in accordance with previous reports.[42,43] On the other hand, the edge sites of 2H-$MoSe_2$ evidenced higher binding energies toward all of the LiPS due to localized edge states,[36] including solid species, which are at least twice that observed in the case of the 2H-$MoSe_2$ basal plane.

On the other hand, during the early lithiation process, the electron transfer process from adsorbate was found to distort the 2H structure, leading to a reconstructed thermodynamically stable metallic 1T′ phase.[41,44] In the simulations, the polysulfides' binding energies at various lithiation stages toward the stable distorted 1T′ structure were evaluated (Figures 1 and S2). We found that with the lithiation process, the binding strength of LiPS species becomes progressively stronger for the 1T′ basal plane in comparison with the 2H phase. To assess the effectiveness of 1T′ phases in suppressing the shuttle effect, we compared the binding energies of higher-order polysulfides Li_2S_n ($n \geq 4$) with the dimethyl ether (DME) electrolyte solvents (0.99−1.20 eV).[45] The stronger adsorption of Li_2S_n ($n \geq 4$) on anchoring materials compared to that of the electrolyte solvent indicates the impediment of the shuttle effect. The calculated adsorption energies clearly illustrate that the basal plane of the reconstructed 1T′ phase is active to effectively immobilize the higher-order polysulfides Li_2S_n ($n \geq 4$); however, the 2H phase cannot endow adequate adsorption strength. Similarly, to gain further insights into the binding characteristics of polysulfides on the edges of 1T′-$MoSe_2$, we constructed energetically stable 50% Se-covered Mo edge sites.[45] The calculated binding energies are shown in Figure 1, and the optimized structures are displayed in Figure

https://doi.org/10.1021/acsami.2c05508
ACS Appl. Mater. Interfaces 2022, 14, 24486−24496

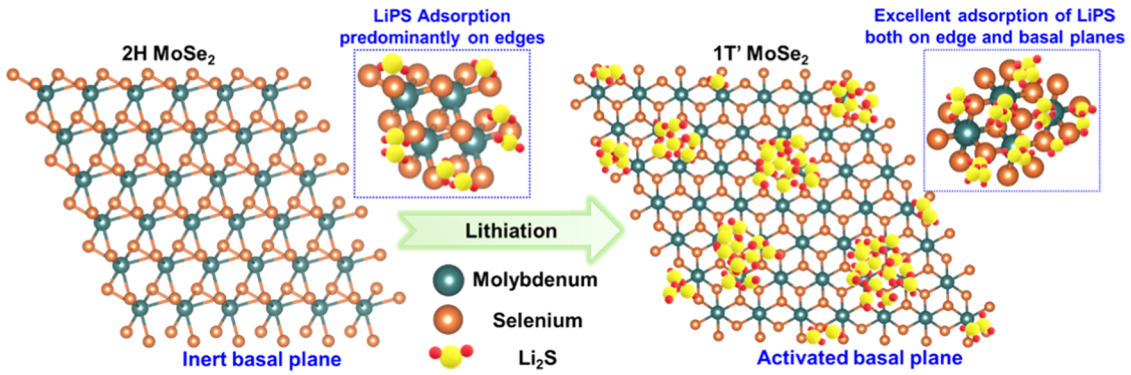

Figure 2. Schematic illustration representing the phase transformation of 2H-$MoSe_2$ into 1T′-$MoSe_2$ upon lithiation and its subsequent influence on the LiPS adsorption.

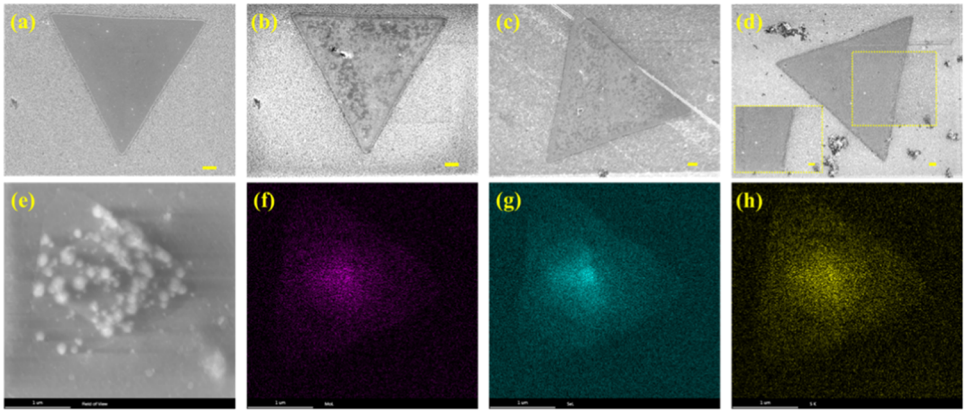

Figure 3. Investigation of LiPS adsorption sites on $MoSe_2$ triangles. (a, b) SEM images of pristine and as-discharged $MoSe_2$ triangles; (c, d) corroborative SEM images of triangles after Li_2S deposition (inset of d shows a zoomed area of the triangle marked in a yellow square), scale bar = 1 μm; and (e−h) SEM and EDAX elemental mapping of molybdenum, selenium, and sulfur elements recorded on a Li_2S-deposited triangle, respectively.

S3. We found that the adsorption strengths of all of the polysulfides towards the edge sites are comparable to those of the basal planes of 1T′-$MoSe_2$. In contrast, it is noteworthy that a strong difference in the edge plane and basal plane activity of 2H-$MoSe_2$ is evident. The strong adsorption of LiPS facilitated via the unsaturated Se dangling bonds at the edges evidences the entrapment of higher-order polysulfides in favor of hindering the shuttle effect. Adsorption energies on the edge sites of the 1T′ and 2H phases toward liquid LiPS are comparable.[5] However, the binding energy of the discharge end product (Li_2S) is certainly higher in the case of the 1T′ edge plane, which can assist in the improvement of sulfur utilization. More importantly, despite the strong adsorption of polysulfides on both the basal plane and edge sites of 1T′-$MoSe_2$, no chemical decompositions are observed, and polysulfide molecules maintain their structural integrity. Based on our simulation results, we predict that both the basal plane and edges of 1T′-$MoSe_2$ are expected to be active for polysulfide immobilization and catalytic conversion of polysulfides, as depicted in Figure 2.

2.2. LiPS Interaction with the Active Sites of 1T′-$MoSe_2$. To corroborate DFT predictions, we performed ex situ SEM and XPS studies to visualize LiPS adsorption and unveil the phase transformation mechanism, respectively. Initially, for SEM purposes, few-layered $MoSe_2$ nanosheets were grown using chemical vapor deposition (CVD) on the SiO_2/Si substrate according to the procedure elucidated in our previous report.[46] These ultrathin triangular nanosheets were subsequently characterized using Raman spectroscopy using a 532 nm green laser. The corresponding Raman spectra showed characteristic Raman vibration modes at ∼245 and 280 cm^{-1} corresponding to the strong out-of-plane A_{1g} and $E_{2g}{}^1$ modes of 2H-$MoSe_2$ (Figure S4).[47,48] A slight blue shift and red shift in A_{1g} and E_{2g} Raman peaks, compared with the typical $MoSe_2$ flakes, can be ascribed to the increase in the thickness of $MoSe_2$ flakes and indicate the presence of multilayers.[49,50] Further, to visualize $MoSe_2$ active sites' influence on the Li_2S_x adsorption and their catalytic conversion reactions, as-grown nanoflakes were transferred onto aluminum patterned electrodes on a SiO_2/Si wafer. After transferring the flakes onto the patterned substrate, wire bonding was carried out to get proper electrical connections for further electrochemical studies. Two-electrode electrochemical cells were assembled with $MoSe_2$ chips as working electrodes and metallic Li as a counter/reference electrode in a 10 mM Li_2S_4 catholyte solution containing 1 M LiTFSI and 0.1 M $LiNO_3$ in tetraethylene glycol dimethyl ether (TEGDME) as the solvent. To understand the Li_2S_x adsorption on catalytic sites of the flakes, galvanostatic discharge was performed at a current rate of 1 μA for 6 h. After deposition, the flakes were carefully removed from the LiPS solution, subsequently washed with the TEGDME solvent, and dried under vacuum overnight. Then, the ex situ SEM images of several $MoSe_2$ triangles recorded after the discharge process, Figure 3a−d, depict the formation

https://doi.org/10.1021/acsami.2c05508
ACS Appl. Mater. Interfaces 2022, 14, 24486−24496

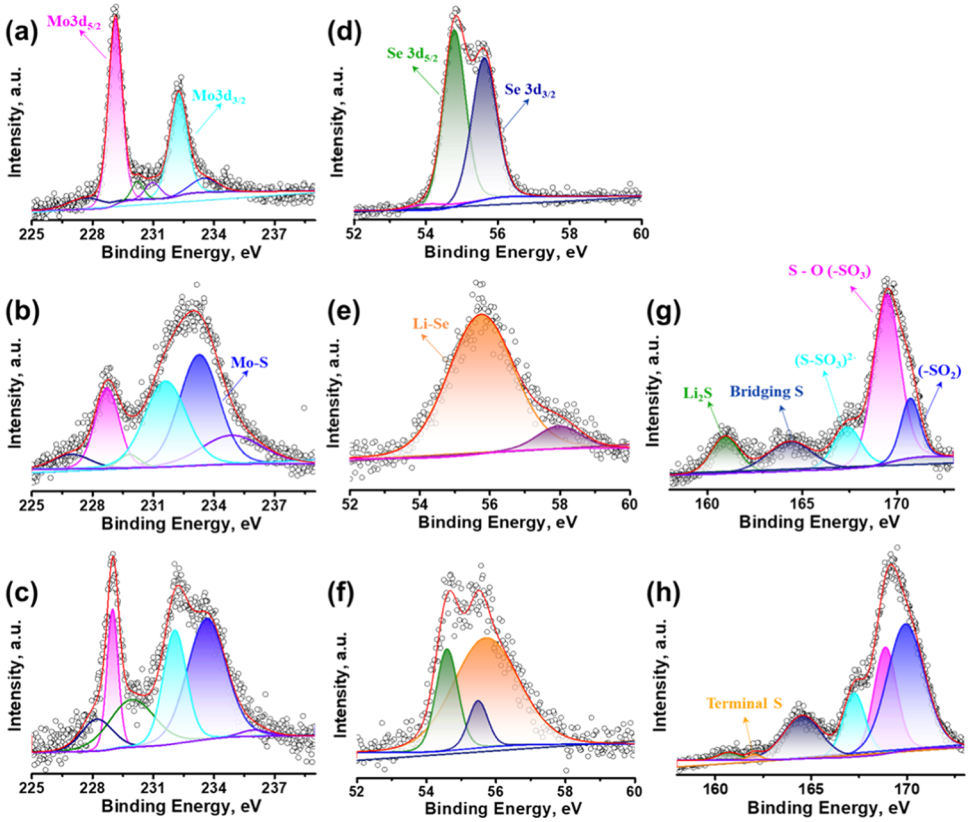

Figure 4. High-resolution XPS spectra of the 1T′-$MoSe_2$ (a−c) Mo, (d−f) Se, and (g, h) S elements under (a, d) pristine, (b, e, g) discharged, and (c, f, h) charged conditions.

of polysulfide deposits all over the flakes (the SEM images of triangles in Figure 3c,d before deposition are shown in Figure S5). Previously, it was elucidated that LiPS preferentially adsorb along the edges of TMDs and undergo further deposition, which was anticipated to be due to their unsaturated active sites, while leaving most of the inactive basal plane (center part of the triangle) unused.[11] On the other hand, in our case, LiPS deposition was found to occur on the entire triangle as evidenced by the white deposits throughout the surface (Figure 3b,c). Based on these facts, we hypothesize that LiPS undergoes adsorption on both the basal and edge planes of 1T′-$MoSe_2$, where further conversion reactions are expected to proceed. Such a phenomenon can be explained as follows: while Mo−S interactions are common, it is noteworthy here that the highly exposed and more catalytic Se sites[11] throughout the basal planes contribute toward the adsorption of Li_2S_x (through Li−Se interactions) on basal as well as edge planes. Moreover, the activation of the 1T′ phase of $MoSe_2$ during the discharge process and its corresponding excellent electronic structure and physical properties might contribute to enhanced Li_2S_x adsorption, as demonstrated by DFT studies. However, the amount of polysulfide deposition on 1T′-$MoSe_2$ flakes is strongly dependent on the time of galvanostatic discharge. Upon discharge of another $MoSe_2$ chip for 12 h, granular and large amounts of solid discharge end product deposits were observed all over the $MoSe_2$ triangle. Further, energy-dispersive X-ray analysis (EDAX) elemental mapping further confirms the complete coverage of sulfur on the edge as well as basal planes of nanosheets, which support the strong LiPS adsorption and their conversion on 1T′-$MoSe_2$, as shown in Figure 3f−h.

Further, to gain insights into the phase transformations occurring in 2H-$MoSe_2$ nanosheets and decipher their effect on the binding strength of LiPS species, we performed systematic XPS analysis on pristine, discharged, and charged Li−S cathodes with $MoSe_2$ nanosheets. Though the CVD process is well known to get high-quality TMD nanosheets with definite morphology and layer orientation on the SiO_2 substrate, it cannot be directly translated into Li−S batteries because of the nonconducting nature of the growth substrate. Hence, we grew $MoSe_2$ triangles onto a conductive carbon cloth (CC) by appropriate control of the CVD process parameters to be used for subsequent studies.[51,52] These CVD-grown $MoSe_2$ triangular nanosheets on CC were systematically characterized using SEM, EDAX, and X-ray diffraction (XRD). Figure S6a,b shows the SEM images of $MoSe_2$ triangular nanosheets at different magnifications on CC. SEM images elucidate the triangular structure of $MoSe_2$ on carbon fiber, whereas EDAX mapping confirms the distribution of Mo and Se on carbon fiber (Figure S6c−e). The XRD pattern of CC with $MoSe_2$ (Figure S7) demonstrates a strong peak at 26°, which can be ascribed to the (002) plane of the carbon cloth. Furthermore, several peaks at 13.7, 31.8, and 37.2° corresponding to the (002), (100), and (103) planes of $MoSe_2$, respectively, were observed. The as-grown $MoSe_2$ on CC was used as a sulfur cathode host for XPS and electrocatalytic property evaluation studies.

First, to ascertain the electrochemical phase transformation occurring in the $MoSe_2$ triangles into 1T′-$MoSe_2$, we performed ex situ XPS studies (Figure 4) and compared them with bulk $MoSe_2$ (Figure S8). All of the XPS spectra peak positions were centered with respect to the carbon C 1s peak

https://doi.org/10.1021/acsami.2c05508
ACS Appl. Mater. Interfaces 2022, 14, 24486−24496

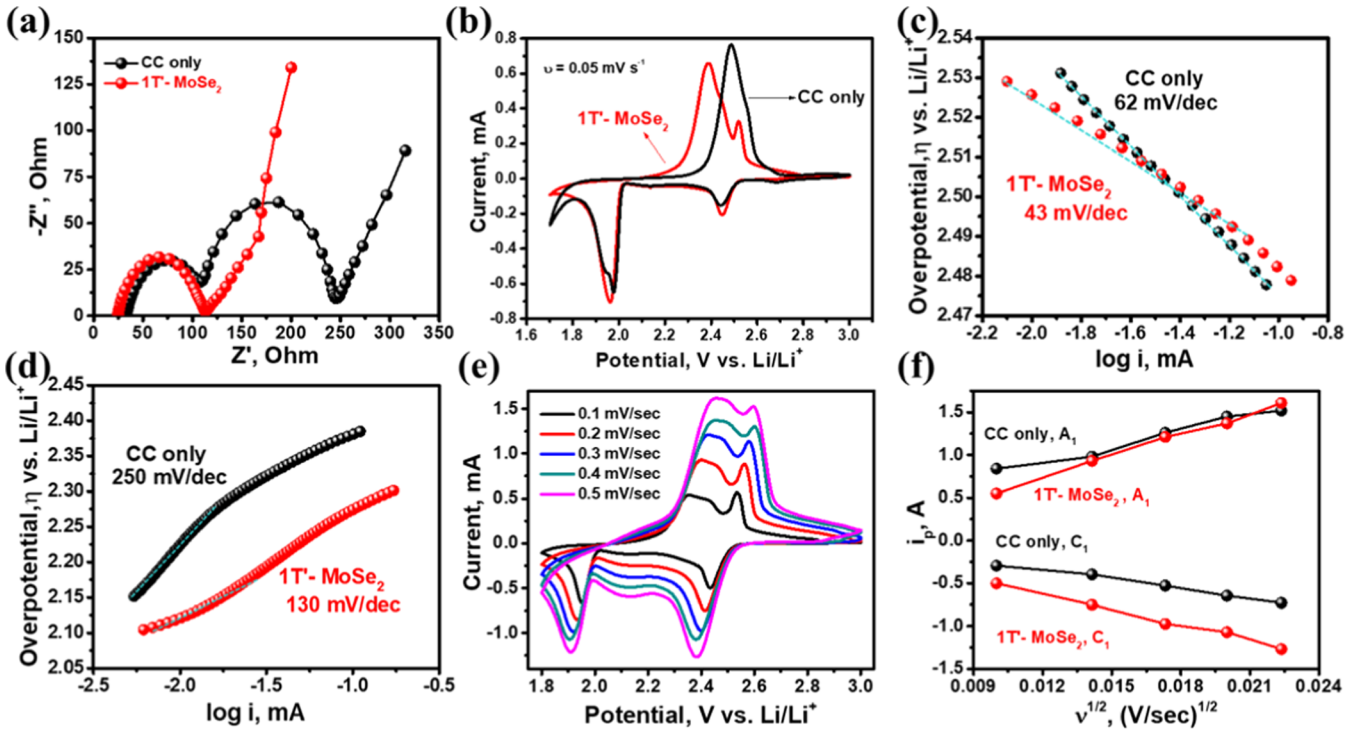

Figure 5. Evaluation of electrocatalytic properties. (a) Nyquist plot and (b) cyclic voltammograms recorded at a scan rate of 0.05 mV s^{-1} on the CC only and CC with $MoSe_2$ electrodes; Tafel slopes derived from the cyclic voltammetry (CV) for (c) reduction reaction at ∼2.5 V and (d) oxidation reaction at ∼2.3 V; (e) cyclic voltammograms recorded at various scan rates on the CC with the $MoSe_2$ electrode (CVs as a function of the scan rate for the CC only electrode are presented in the SI); and (f) linear relationship between cathodic and anodic peak currents and the square root of scan rates for both electrodes.

position at 284.6 eV. As shown in Figures 4a and S8a, the Mo 3d XPS spectra of both the pristine $MoSe_2$ triangle sample and bulk 2H-$MoSe_2$ were resolved into two predominant peaks centered at 229.1 and 232.2 eV corresponding to two core levels Mo^{4+} $3d_{5/2}$ and Mo^{4+} $3d_{3/2}$, respectively, which typically represent the 2H phase of $MoSe_2$. Interestingly, upon discharging the $MoSe_2$ triangles (Figure 4b), the two original Mo 3d peaks were found to move to lower binding energies at 228.7 and 231.5 eV with a negative shift of around 0.4 and 0.7 eV, respectively, indicating the phase transformation of the 2H to 1T′ phase.[28,53] In addition, a strong new peak was observed at a binding energy of 233.3 eV, which can be attributed to the formation of the Mo−S bond, indicating LiPS species' binding to Mo atoms. On the other hand, the Mo 3d spectrum of bulk 2H-$MoSe_2$ (Figure S8b) still demonstrated the two peaks but with a slight positive shift (229.25, 232.28 eV). Similarly, the Se 3d doublet peak of the $MoSe_2$ triangle and bulk 2H-$MoSe_2$ (Figures 4d and S8d, respectively) was deconvoluted into two characteristic peaks at 54.8 and 55.6 eV resulting from Se^{2-} $3d_{5/2}$ and Se^{2-} $3d_{3/2}$, belonging to the 2H phase of $MoSe_2$.[28,54,55] In the discharged samples of triangular $MoSe_2$ (Figure 4e), the typical Se 3d peak was found to disappear, and only one peak at a higher binding energy (∼55.7 eV) was observed, indicating a strong binding of Se with Li to form Li_2Se, thus anchoring LiPS. Contrarily, the Se 3d spectra of bulk 2H-$MoSe_2$ showed a small positive shift, indicating that certain valance electrons transferred from negatively charged Se to positively charged Li. While small positive shifts in both Mo and Se of bulk 2H-$MoSe_2$ suggest some interaction between these elements and S and Li, no phase-change-related shifts analogous to 1T′-$MoSe_2$ were noted.[56]

These results indicate that upon discharging, triangular 2H-$MoSe_2$ completely reconstructs into 1T′-$MoSe_2$, which activates the basal plane contributing to the effective anchoring of LiPS and their further conversion. Upon charging, certain 1T′-$MoSe_2$ can be transformed back into the 2H phase, and over repeated cycling, the 2H phase is expected to completely convert into the 1T′ phase. To corroborate, we have analyzed the Mo 3d spectra of charged samples (Figure 4c), which exhibited the characteristic peaks with a slight positive shift in their binding energies. The Se 3d spectrum (Figure 4f) also demonstrated the typical Se $3d_{5/2}$ and Se $3d_{3/2}$ peaks at corresponding binding energies along with the Li−Se bond. In the S 2p spectrum of the discharged bulk 2H-$MoSe_2$ (Figure S8g) sample, a strong peak at 161 eV was observed corresponding to the formation of a discharge end product (Li_2S). However, the S 2p spectrum of the charged sample still showed a significant presence of the Li_2S peak, demonstrating the inferior capability of 2H-$MoSe_2$ in converting the discharge end products effectively. It is noteworthy to mention that, during discharge, the S 2p spectrum (Figure 4g) demonstrated a peak at 164.3 eV corresponding to typical bridging sulfur of LiPS and another peak at ∼161 eV, which can be ascribed to the discharge end product Li_2S.[57,58] Moreover, in the charged samples (Figure 4h), the peak corresponding to Li_2S was found to disappear and the formation of a strong peak corresponding to bridging sulfur along with a new peak at ∼162 eV representing terminal sulfur was noted. Such an observation represents an effective conversion of an active material (Li_2S_8) into charge/discharge end products.

Further, we performed the Bader charge and charge density difference analysis to elucidate the electronic and electrocatalytic behavior of $MoSe_2$ upon LiPS adsorption. The charge

https://doi.org/10.1021/acsami.2c05508
ACS Appl. Mater. Interfaces 2022, 14, 24486−24496

density plot for the representative cases such as Li_2S, Li_2S_4, and Li_2S_8 on the 1T′ phase is presented in Figure S9. From the figure, we find that the electrons are accumulated mainly on the $MoSe_2$ substrate from the Li_2S_n clusters, and the observation is directly corroborated with the charge transfer data. The density of states calculations performed to understand the electronic properties, as shown in Figure S10, depict the metallic conducting nature of the 1T′ phase. The retention of the conducting behavior even after Li_2S_n adsorption is conducive to electronic conduction and superior catalytic activities of lower-order polysulfides. Overall, the $MoSe_2$ phase transformation mechanism and its effect on LiPS adsorption can be explained as follows. (i) Initially, upon discharge of the Li−S cell, the 2H phase of $MoSe_2$ converts into the 1T′ phase due to Li^+ intercalation. While the 2H phase is typically semiconducting, the 1T′ phase is highly metallic in nature; particularly, unlike the 2H phase, both the basal and edge planes are active in the 1T′ phase, which further boosts the chemical and electrocatalytic activities of $MoSe_2$.[59] (ii) The 1T′-$MoSe_2$ binds excellently with both the sulfur and Li ends of LiPS, via Mo−S and Li−Se interactions due to the high adsorption energy of both edge and basal planes of 1T′ toward LiPS as revealed by DFT simulations; besides, the enhanced active sites efficiently convert the anchored LiPS into charge/discharge end products, which is crucial for the reversibility of the cell. (iii) Finally, after first charging, a certain 1T′ phase retransformed into 2H-$MoSe_2$ while still capturing LiPS on the cathode surface via similar interactions as observed during discharge, thus efficiently curbing the LiPS shuttle. After confirming the beneficial role of these phase transformations in the LiPS adsorption, next, it is imperative to investigate this material's electrocatalytic behavior on the overall LiPS redox process.

2.3. Evaluation of the Electrocatalytic Properties of 1T′-$MoSe_2$ on LiPS Redox Reactions. To prove the electrocatalytic capability of 1T′-$MoSe_2$ toward LiPS, we fabricated a standard coin cell as per the procedure described in the Experimental Section. To evaluate the electrochemical behavior of the as-prepared cells with and without $MoSe_2$, electrochemical impedance spectroscopy measurements were carried out in the frequency range of 1 MHz to 100 mHz. Figure 5a depicts the corresponding Nyquist plots, which show an intercept on the real axis corresponding to the ohmic resistance (R_s) followed by a semicircle in the high-frequency region typically ascribed to the charge transfer resistance (R_{ct}). A second semicircle was noted in the middle-frequency region (R_f) predominantly on the cells with only CC electrodes; the mere existence of this semicircle in a fresh cell represents the deposition of an insoluble solid film of Li_2S/Li_2S_2 on the anode surface, produced by a reaction between the Li-metal anode and the LiPS (formed during self-discharge), which migrate from the cathode to anode.[60,61] In the low-frequency region, an inclined line (Warburg impedance W_o) was noted, which represents the Li-ion diffusion within the cathode material.[62] The impedance spectra were further modeled using an equivalent circuit (Figure S11, and fitting parameters are elucidated in Table S1), and given the rough/porous surface of the CC electrode, a constant phase element was chosen along with resistance components during the modeling.[63] While the R_s and R_{ct} for both as-prepared cells are identical, it is noteworthy that the value of R_f for the 1T′-$MoSe_2$ is almost negligible (∼2.1 Ω), compared to that of the CC electrode (122.5 Ω). More importantly, given that the active material was in the form of liquid LiPS (Li_2S_8), such an observation demonstrates that the LiPS shuttle process was mitigated by $MoSe_2$ nanosheets through strong interactions.

Next, to decipher the electrocatalyst's influence on the LiPS redox and liquid−solid conversion reaction kinetics, the Li−S cells were probed via cyclic voltammetry (CV). Figure 5b shows the CV recorded at a scan rate of 0.05 mV/s on two coin cells with/without $MoSe_2$ loading. The CV of CC alone demonstrated two characteristic reduction peaks at 2.43 (I) and 1.96 (II) V, corresponding to the conversion of long-chain LiPS to medium-chain LiPS and their subsequent conversion to discharge end products (Li_2S/Li_2S_2). On the other hand, upon incorporating $MoSe_2$, a clear anodic shift of the reduction peak I (∼2.45 V) and higher currents on both reduction processes were noted. Further, during the anodic scan, a broad oxidation peak centered at 2.49 V corresponding to the conversion of Li_2S to LiPS/S in a single step was observed in the case of CC. Interestingly, a noticeable cathodic shift and split in the anodic peak (2.38 and 2.52 V) were seen on $MoSe_2$, indicating the catalytic effect toward converting lower chain polysulfide first to upper chain polysulfide and then to elemental sulfur (S_8). The potential difference ($\Delta E_p = E_{pa1} - E_{pc2}$) between the first anodic peak (E_{pa1}) and the second cathodic peak (E_{pc2}) was found to be 0.53 and 0.41 V for the CC and $MoSe_2$ cells, respectively. It is noteworthy that a decrease in ΔE_p typically represents a decrease in cell polarization between the LiPS redox reaction. Similarly, CV studies were also performed on bulk 2H-$MoSe_2$ to distinguish the effect of 1T′-$MoSe_2$ (Figure S12). The CV of bulk 2H-$MoSe_2$ demonstrated two characteristic reduction peaks at 2.45 and 1.97 V corresponding to the conversion of long-chain LiPS to medium-chain LiPS and their subsequent conversion to discharge end products. On the other hand, during the anodic scan, 2H-$MoSe_2$ demonstrated two oxidation peaks at 2.43 and 2.53 V, indicating a two-step oxidation behavior. However, it is evident that 1T′-$MoSe_2$ showed stronger cathodic shifts and higher peak currents compared to 2H-$MoSe_2$, indicating the higher catalytic behavior of 1T′-$MoSe_2$ toward LiPS conversion.

Also, to elucidate the electrocatalytic effect of 1T′-$MoSe_2$, we performed a Tafel slope analysis, as shown in Figure 5c,d. The 1T′-$MoSe_2$ shows a Tafel slope value of 43 mV/dec for the reduction of Li_2S_8 (∼2.4 V), which was very low compared to that of CC alone (62 mV/dec). Besides, the exchange current density (i_0) obtained from extrapolation of the current axis in the Tafel plot was higher on the 1T′-$MoSe_2$ (0.16×10^{-3} A/cm^2) surface compared to the CC (0.09×10^{-3} A/cm^2). Furthermore, the Tafel slope and i_0 for the oxidation process (∼2.4 V) were found to be 250, 130 mV/dec and 0.0016, 0.0022 mA/cm^2 for the CC and 1T′-$MoSe_2$ electrodes, respectively. The obtained low Tafel slope and higher exchange current density values of the 1T′-$MoSe_2$ surface during the reduction and oxidation processes (Table S2) indicate a facile conversion of higher-order LiPS (Li_2S_8) into medium-chain LiPS (liquid/liquid) and conversion of discharge end products effectively into charge products, respectively.

Further, given that fast Li^+ diffusion can facilitate the LiPS conversion process, we calculated the Li^+ diffusion coefficient to gain insights into the role of 1T′-$MoSe_2$ in LiPS redox reactions. Figures 5e and S13 show the CVs of the CC with and without $MoSe_2$ electrodes, respectively, recorded at different scan rates ranging from 0.1 to 0.5 mV/s, and Figure 5f depicts the corresponding peak currents vs square root of

https://doi.org/10.1021/acsami.2c05508
ACS Appl. Mater. Interfaces 2022, 14, 24486−24496

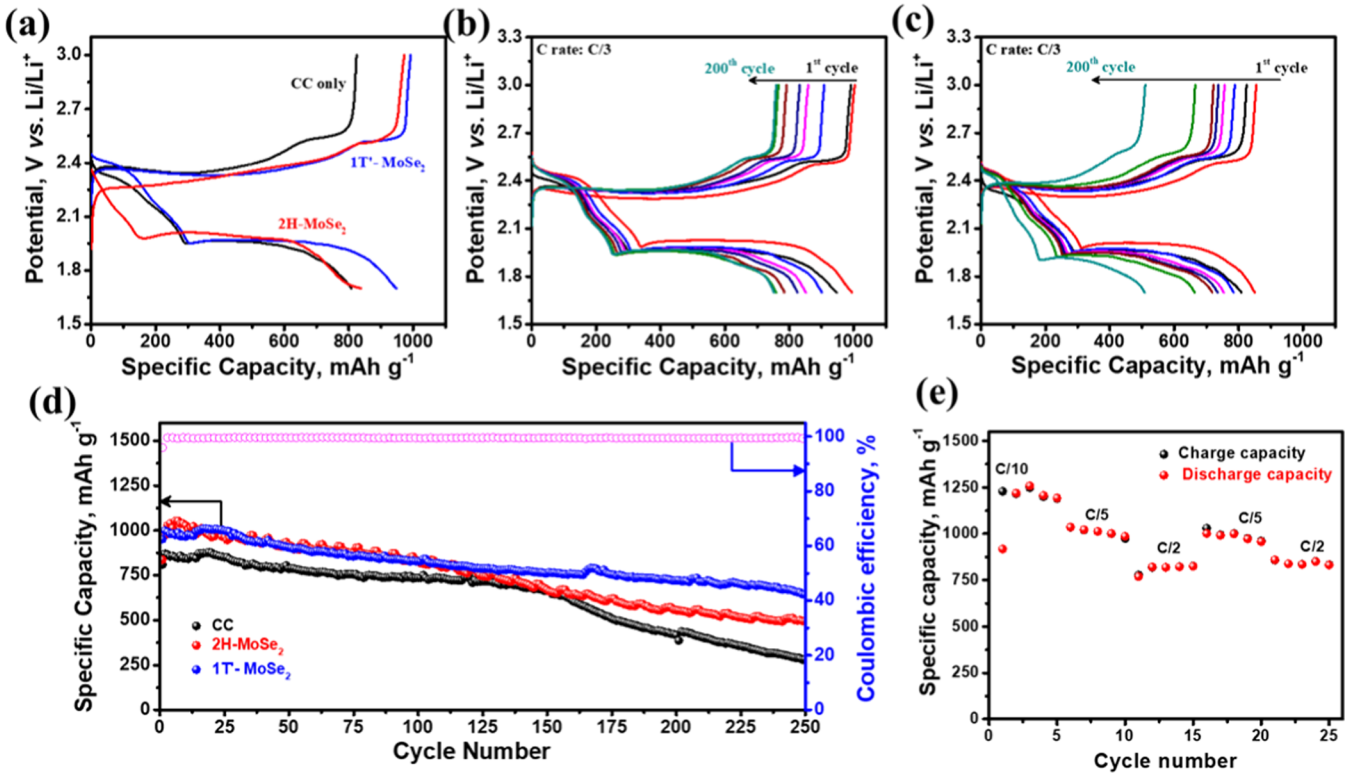

Figure 6. Electrochemical characterizations. (a) Voltage vs specific capacity profiles depicting the cell polarization; (b, c) galvanostatic charge−discharge profiles of the 1T′-$MoSe_2$ and CC only electrodes; (d) long cycling performance of both electrodes and Coulombic efficiency of the 1T′-$MoSe_2$ electrode; and (e) rate capability studies carried out on the cell with the 1T′-$MoSe_2$ electrode.

the scan rates. It can be observed that the cathodic and anodic peak currents (i_p) of both electrodes demonstrated an excellent linear relationship with the square root of scan rates ($\nu^{1/2}$), indicating a diffusion-controlled process. Hence, Li^+ diffusivity was calculated by the Randles−Sevcik equation: $i_p = (2.65 \times 10^5)\ n^{1.5}\ S\ D_{Li}{}^{+0.5}\ \Delta C_{Li}\ \nu^{0.5}$, where I_p is the peak current, n is the number of electrons, S is the geometric area of the electrode, $D_{Li}{}^+$ is the Li-ion diffusion coefficient, ΔC_{Li} is the Li-ion concentration in the cathode, and ν is the scan rate. The D_{Li+} values calculated for the CC with $MoSe_2$ electrode were found to be higher than those for the CC only electrode (Table S3). This can be explained as follows: the CC only electrodes allow for weak interactions toward LiPS adsorption with a subsequent buildup of insulating charge/discharge end products leading to a low Li^+ diffusivity. On the other hand, highly conductive 1T′- $MoSe_2$ can aid in very fast Li^+ diffusion, representing superior catalytic activity, thus enabling effective LiPS conversion. In effect, these kinetic parameters and Li^+ diffusion coefficients are a clear indication of the catalytic effect of $MoSe_2$ on polysulfide conversion reactions.

Next, to appraise the Li−S cycling performance, galvanostatic charge/discharge studies were performed on 1T′-$MoSe_2$ and were compared with bulk 2H-$MoSe_2$ and CC alone cells, at a constant current rate of 0.33C in the potential window between 3.0 and 1.7 V vs Li/Li^+. From Figure 6a, it can be observed that the CC and 2H-$MoSe_2$ electrodes demonstrated two distinct discharge plateaus at 2.33, 1.96 V and 2.18, 2.00 V, respectively. Similarly, 1T′-$MoSe_2$ showed two discharge plateaus at 2.40 and 1.97 V. These plateaus can be attributed to the reduction of Li_2S_8 to medium-chain LiPS (Li_2S_n, $n > 4$) and subsequently to short-chain LiPS/discharge end products (Li_2S_n, $n = 1-3$). More importantly, a reduced polarization can be observed in the case of the 1T′-$MoSe_2$ compared to the CC and 2H-$MoSe_2$ electrodes, depicting enhanced redox kinetics for LiPS conversions on $MoSe_2$ nanosheets. Further, it can be noted that the 1T′-$MoSe_2$ electrode delivered a discharge capacity of ∼1000 mAh g^{-1} in the initial cycles and demonstrated an excellent capacity retention behavior for over 250 cycles, with limited changes in the polarization (Figure 6b). On the other hand, the CC electrode delivered an initial capacity of only ∼850 mAh g^{-1} at 0.33C and displayed a sharp decay in its capacity with a constant increase in the cell polarization even within 200 cycles (Figure 6c).

Furthermore, to appraise the changes in R_{ct} and R_f under charge/discharge conditions, electrochemical impedance spectroscopy (EIS) spectra were collected for both cells in fully discharged and charged conditions, as shown in Figure S14. Typically, R_f was also associated with the generation of LiPS and their subsequent transformation into charge/discharge end products on the positive electrode material.[64,65] Accordingly, after the first discharge, R_{ct} significantly reduced for both cells, but R_f was found to be 245.1 and 2.3 Ω for the CC and 1T-$MoSe_2$ cells, respectively, and the increase in the size of the mid-frequency semicircle for the CC electrode depicts the dissolution of as-formed LiPS into the electrolyte. Subsequently, after the first charge, R_{ct} for the 1T′-$MoSe_2$ electrode (8.2 Ω) was very small, indicating a facile electron transfer process compared to that of CC (150 Ω). Furthermore, EIS spectra were collected for both cells after 10 cycles, where the CC electrode demonstrated two clear semicircles while only one clear depressed semicircle was noted on 1T′-$MoSe_2$. Interestingly, for identical cells, R_{ct} for 1T′-$MoSe_2$ was noted to be only half that of the CC cell, which can be attributed to the enhanced conductivity of $MoSe_2$. Even

https://doi.org/10.1021/acsami.2c05508
ACS Appl. Mater. Interfaces 2022, 14, 24486−24496

after 10 cycles, the R_f of 1T′-$MoSe_2$ was at least 8 times lower than the CC electrode, indicating the uniform deposition of charge/discharge products on its surface over cycling, while the Li^+ diffusion to the deposits is facilitated. Overall, from the impedance analysis, it can be concluded that $MoSe_2$ nanosheets offer an excellent electronically conductive sulfur host matrix, which not only curbs LiPS dissolution into the electrolyte but also enables a stable interface, essential for high rate capability and long cycling performance in Li−S batteries.

Figure 6d evidences the cycling stability at a 0.33C rate, where an average stable capacity of >800 mAh g^{-1} was realized for 1T′-$MoSe_2$ for over 250 cycles. More importantly, the cell displayed an excellent Coulombic efficiency of 99.6% throughout cycling with a minimal average capacity loss of only 0.15% per cycle due to the effective conversion of polysulfides on the electrocatalytically active $MoSe_2$ surface. While the 2H-$MoSe_2$ electrode delivered an average capacity of ∼750 mAh g^{-1} and cycling stability comparable to that of 1T′-$MoSe_2$ until 125 cycles, the capacity quickly faded after that possibly due to the catalytic deactivation effect.[66] On the other hand, while the CC delivered a stable capacity for certain cycles, a sudden drop in capacity was observed after 150 cycles, which quickly declined to only ∼280 mAh g^{-1} at the end of the 250th cycle. The average capacity demonstrated by CC without $MoSe_2$ was only ∼630 mAh g^{-1}, with an average capacity decay of 0.41% per cycle. Over the cycles, charge−discharge end products typically accumulate on the electrode surface, and given the inability of the carbon surface to efficiently convert them in the subsequent cycles, such a pile-up of insulating products decreases the active surface area leading to fast capacity fade. Contrarily, the stable capacity on 1T′-$MoSe_2$ demonstrates its superior catalytic behavior toward LiPS conversion over several cycles.

Finally, the electrochemical behavior of 1T′-$MoSe_2$ at different C rates was evaluated, as shown in Figure 6e. Herein, 1T′-$MoSe_2$ delivered superior specific capacity to that of the CC electrode at three different C rates of 0.1C, 0.2C, and 0.5C. For instance, a discharge capacity of 1220, 1033, and 820 mAh g^{-1} was obtained at 0.1, 0.2, and 0.5C, respectively. Similar capacities were derived from the cell even after retaining C rates of 0.2 and 0.5C in the subsequent cycles (15−20 cycles). Hence, electrocatalytically active materials, like phase-transformed $MoSe_2$, exhibit superior specific capacity and rate capability over pristine CC and are essential to enhance LiPS reversibility and reaction kinetics. Table S4 compares various electrochemical performance metrics of state-of-the-art TMD cathodes with the current 1T-$MoSe_2$. It is evident that 1T′-$MoSe_2$ electrodes delivered the highest Coulombic efficiency compared to any other contemporary electrodes, even at a reasonable C rate of 0.33C. On the other hand, some of the other TMDs demonstrated higher specific capacity, which can be a result of the highly conductive carbonaceous matrix, such as reduced graphene oxide (rGO) and carbon nanotubes (CNTs), which were used as a host for catalytic TMD materials. These studies suggest that a combination of the proposed 1T′-$MoSe_2$ materials with highly conductive carbons can further enhance the performance of the Li−S batteries.

3. CONCLUSIONS

In summary, we have demonstrated the influence of phase transformation occurring in TMDs during Li−S discharge on LiPS adsorption and their subsequent conversion reactions. Theoretical calculations unveiled that the reconstructed stable and metallic 1T′ phase from conventional 2H-$MoSe_2$ activates the basal planes. More importantly, such activated basal planes exhibit robust adsorption capabilities toward intermediate LiPS in addition to the inherently active edge planes. Systematic scanning electron microscopy images revealed the facilitated adsorption and deposition of LiPS all over the $MoSe_2$ triangular structures. Furthermore, spectroscopy studies of pristine and cycled samples of $MoSe_2$ nanosheets evidenced the 2H −1T′ phase transformation and Mo/Se sites' contribution on the edge and basal planes toward LiPS anchoring. Adsorbed LiPS undergoes facile solid−liquid-solid conversion as evidenced by the detailed electrochemical and kinetic analysis in terms of Tafel slope, exchange current density, and Li^+ diffusion coefficient measurements. Finally, due to the enhanced adsorption and catalytic conversion of LiPS, a very high initial capacity of ∼1000 mAh g^{-1} was realized at 0.33C with an excellent Coulombic efficiency of over 99.6% for over 250 cycles. Hence, exploration of the TMD phase transformational effect on Li−S battery performance is the first of its kind and provides a great avenue to design phase-engineered materials for next-generation battery technologies.

4. EXPERIMENTAL SECTION

4.1. Materials and Methods. *4.1.1. Growth of $MoSe_2$ Triangles.* Initially, $MoSe_2$ nano triangles were grown on a SiO_2 substrate using a CVD method, as per the procedure described in our previous study.[46] Briefly, MoO_3 powder was initially sprinkled onto a SiO_2 substrate in an alumina boat, which was placed in the center of the CVD reactor (high-temperature zone) in a 2-inch quartz tube; simultaneously, another boat consisting of selenium pellets was placed in the low-temperature zone (200−270 °C) upstream relative to the gas flow direction. Prior to the growth process, the furnace was flushed out with high-purity Ar gas for 20 min to exhaust all of the air. Later, the furnace temperature was raised to 750 °C with a ramp speed of 55 °C/min, and that temperature was maintained for 25 min under a continuous flow of a mixture of Ar (80 sccm) and H_2 (20 sccm) gases.

4.1.2. Growth of $MoSe_2$ on Carbon Cloth. The growth process of $MoSe_2$ triangles on CC was carried out by initially sprinkling MoO_3 powder on a porcelain boat. The CC was then placed on top of the boat and loaded into the center of a 2-inch quartz tube; another boat with ∼500 mg of selenium pellets was loaded in a tube such that when the temperature of the center zone reaches 750 °C, the temperature of the selenium boat ranges between 200 and 270 °C. A mixture of hydrogen (20%) and argon was used as a carrier gas, which creates a reducing atmosphere during the deposition process. Recently, Cao et al. used Wulff's construction to exemplify the shape as a function of chemical composition,[67] where the triangular-based crystal shape contains more chalcogens (S or Se); these triangular nanoclusters were found to be more catalytic.[68] Therefore, selenium introduction time plays a very crucial role to get the triangular structure, whereas hydrogen helps to reduce MoO_3 powder to MoO_x-Se and then to $MoSe_2$.[69]

4.2. Material Characterization. FE-SEM images (JEOL JSM-7600) were collected at an operating voltage of 2 kV to study the morphology of $MoSe_2$ nanosheets. X-ray diffraction (XRD) patterns of the as-prepared samples were collected at a scan rate of 0.05 s^{-1} using Cu Kα radiation (Rigaku Miniflex II X-ray diffractometer). Raman spectra were recorded by the Andor Shamrock 500i system with a 532 nm green laser (Nd: YaG source). The X-ray photoelectron spectra of the as-prepared materials and cycled electrodes were collected using a ThermoFisher Scientific NEXSA UV and X-ray Photoelectron Spectrometer, and open-source XPS peak fit 4.1 software was used for deconvoluting the spectra.

4.3. Cell Fabrication and Electrochemical Measurements. Standard 2032-coin cells were assembled inside an argon-filled

https://doi.org/10.1021/acsami.2c05508
ACS Appl. Mater. Interfaces 2022, 14, 24486−24496

glovebox (oxygen and moisture levels maintained below 0.1 ppm) to study the electrochemical performance of $MoSe_2$ against sulfur and intermediate LiPS redox reactions. The carbon cloth with/without $MoSe_2$ loading was cut into circular disks each with a diameter of 12.7 mm to be used as a positive electrode and Li metal as an anode. An active material containing catholyte (0.2 M Li_2S_8) was prepared by mixing stoichiometric amounts of Li_2S and S in the tetraethylene glycol dimethyl ether (TEGDME) solvent with effective stirring at 90 °C overnight. Typical coin cells were then assembled using 10 μL of 0.2 M Li_2S_8 as an active material and Celgard as a separator wetted with an appropriate amount of the blank electrolyte (1 M LiTFSI + 0.1 M $LiNO_3$ in TEGDME).

Electrochemical impedance spectroscopy and cyclic voltammetric studies were conducted using a Biologic SP300 bipotentiostat, and the galvanostatic charge−discharge process was performed in the potential range of 3.0−1.7 V in an ARBIN cycle life tester. For the ex situ XPS analysis, a set of two identical coin cells were fabricated according to the procedure described above for each of the $MoSe_2$ triangles anchored on carbon cloth and bulk 2H-$MoSe_2$ on carbon electrodes. One cell from each set was subjected to the discharge process at C/20, while the other was first discharged and then charged at C/20. The cells were then decrimped, the electrodes were washed with a blank TEGDME solvent without any salts, and XPS analyses were then performed on them.

■ ASSOCIATED CONTENT

Supporting Information

The Supporting Information is available free of charge at https://pubs.acs.org/doi/10.1021/acsami.2c05508.

Geometric structures of 2H, 1T′-$MoSe_2$ substrates, and adsorbed LiPS; SEM, Raman, EDAX mappings, and XRD studies on $MoSe_2$ triangles both on a silicon substrate and carbon cloth; ex situ XPS studies on bulk 2H-$MoSe_2$; charge density difference images and density of state plots on the 1T′-$MoSe_2$ substrate; and Nyquist plots of cycled electrodes and associated tables (PDF)

■ AUTHOR INFORMATION

Corresponding Authors

Naresh Kumar Thangavel − *Department of Mechanical Engineering, Wayne State University, Detroit, Michigan 48202, United States;* orcid.org/0000-0002-6604-0211; Email: ge4108@wayne.edu

Md Mahbubul Islam − *Department of Mechanical Engineering, Wayne State University, Detroit, Michigan 48202, United States;* orcid.org/0000-0003-4584-2204; Email: gy5553@wayne.edu

Leela Mohana Reddy Arava − *Department of Mechanical Engineering, Wayne State University, Detroit, Michigan 48202, United States;* orcid.org/0000-0001-6685-6061; Email: leela.arava@wayne.edu

Authors

Kiran Mahankali − *Department of Mechanical Engineering, Wayne State University, Detroit, Michigan 48202, United States;* orcid.org/0000-0003-3540-5350

Sundeep Varma Gottumukkala − *Department of Electrical and Computer Engineering, Wayne State University, Detroit, Michigan 48202, United States*

Nirul Masurkar − *Department of Mechanical Engineering, Wayne State University, Detroit, Michigan 48202, United States*

Rahul Jayan − *Department of Mechanical Engineering, Wayne State University, Detroit, Michigan 48202, United States;* orcid.org/0000-0003-4073-3770

Abdulrazzag Sawas − *Department of Mechanical Engineering, Wayne State University, Detroit, Michigan 48202, United States*

Sudhan Nagarajan − *Department of Mechanical Engineering, Wayne State University, Detroit, Michigan 48202, United States;* orcid.org/0000-0002-3524-5062

Complete contact information is available at: https://pubs.acs.org/10.1021/acsami.2c05508

Author Contributions

§K.M. and S.V.G. contributed equally.

Notes

The authors declare no competing financial interest.

■ ACKNOWLEDGMENTS

This work was supported in part by the National Science Foundation (Grant No. 1751472) and NSF Division of Chemical, Bioengineering, Environmental, and Transport Systems (CBET: 1748363). The authors thank the Lumigen Instrument Centre at Wayne State University for the use of JSM-7600 FE-SEM (NSF: MRI 0922912), PXRD (NSF: MRI 1427926), and XPS (NSF: MRI 1849578) facilities.

■ REFERENCES

(1) Manthiram, A.; Fu, Y.; Chung, S. H.; Zu, C.; Su, Y. S. Rechargeable lithium-sulfur batteries. *Chem. Rev.* **2014**, *114*, 11751−11787.

(2) Bruce, P. G.; Freunberger, S. A.; Hardwick, L. J.; Tarascon, J. M. Li-O_2 and Li-S batteries with high energy storage. *Nat. Mater.* **2012**, *11*, 19−29.

(3) Pang, Q.; Liang, X.; Kwok, C. Y.; Nazar, L. F. Advances in lithium−sulfur batteries based on multifunctional cathodes and electrolytes. *Nat. Energy* **2016**, *1*, No. 16132.

(4) Wang, H.; Zhang, W.; Xu, J.; Guo, Z. Advances in polar materials for lithium−sulfur batteries. *Adv. Funct. Mater.* **2018**, *28*, No. 1707520.

(5) Pang, Q.; Kundu, D.; Cuisinier, M.; Nazar, L. Surface-enhanced redox chemistry of polysulphides on a metallic and polar host for lithium-sulphur batteries. *Nat. Commun.* **2014**, *5*, No. 4759.

(6) Li, J.; Qu, Y.; Chen, C.; Zhang, X.; Shao, M. Theoretical investigation on lithium polysulfide adsorption and conversion for high-performance Li−S batteries. *Nanoscale* **2021**, *13*, 15−35.

(7) Ng, S. F.; Lau, M. Y. L.; Ong, W. J. Lithium−Sulfur Battery Cathode Design: Tailoring Metal-Based Nanostructures for Robust Polysulfide Adsorption and Catalytic Conversion. *Adv. Mater.* **2021**, *33*, No. 2008654.

(8) Mahankali, K.; Nagarajan, S.; Thangavel, N. K.; Rajendran, S.; Yeddala, M.; Arava, L. M. R. Metal-Based Electrocatalysts for High-Performance Lithium-Sulfur Batteries: A Review. *Catalysts* **2020**, *10*, 1137.

(9) Babu, G.; Ababtain, K.; Ng, K. Y.; Arava, L. M. Electrocatalysis of lithium polysulfides: current collectors as electrodes in Li/S battery configuration. *Sci. Rep.* **2015**, *5*, No. 8763.

(10) Al Salem, H.; Babu, G.; Rao, C. V.; Arava, L. M. Electrocatalytic Polysulfide Traps for Controlling Redox Shuttle Process of Li-S Batteries. *J. Am. Chem. Soc.* **2015**, *137*, 11542−11545.

(11) Babu, G.; Masurkar, N.; Al Salem, H.; Arava, L. M. Transition Metal Dichalcogenide Atomic Layers for Lithium Polysulfides Electrocatalysis. *J. Am. Chem. Soc.* **2017**, *139*, 171−178.

(12) Manthiram, A.; Fu, Y.; Su, Y. S. Challenges and prospects of lithium-sulfur batteries. *Acc. Chem. Res.* **2013**, *46*, 1125−1134.

(13) Gao, J.; Li, L.; Tan, J.; Sun, H.; Li, B.; Idrobo, J. C.; Singh, C. V.; Lu, T. M.; Koratkar, N. Vertically oriented arrays of ReS_2 nanosheets for electrochemical energy storage and electrocatalysis. *Nano Lett.* **2016**, *16*, 3780−3787.

(14) Mahankali, K.; Thangavel, N. K.; Gopchenko, D.; Arava, L. M. R. Atomically Engineered Transition Metal Dichalcogenides for Liquid Polysulfide Adsorption and Their Effective Conversion in Li-S Batteries. *ACS Appl. Mater. Interfaces* **2020**, *12*, 27112−27121.
(15) Wang, C.; Sun, L.; Li, K.; Wu, Z.; Zhang, F.; Wang, L. Unravel the Catalytic Effect of Two-Dimensional Metal Sulfides on Polysulfide Conversions for Lithium−Sulfur Batteries. *ACS Appl. Mater. Interfaces* **2020**, *12*, 43560−43567.
(16) Tian, C.; Li, B.; Hu, X.; Wu, J.; Li, P.; Xiang, X.; Zu, X.; Li, S. Melamine Foam Derived 2H/1T MoS_2 as Flexible Interlayer with Efficient Polysulfides Trapping and Fast Li^+ Diffusion to Stabilize Li−S Batteries. *ACS Appl. Mater. Interfaces* **2021**, *13*, 6229−6240.
(17) Thangavel, N. K.; Gopalakrishnan, D.; Arava, L. M. R. Understanding Heterogeneous Electrocatalysis of Lithium Polysulfide Redox on Pt and WS_2 Surfaces. *J. Phys. Chem. C* **2017**, *121*, 12718−12725.
(18) Zhu, C. R.; Gao, D.; Ding, J.; Chao, D.; Wang, J. TMD-based highly efficient electrocatalysts developed by combined computational and experimental approaches. *Chem. Soc. Rev.* **2018**, *47*, 4332−4356.
(19) Wang, H.; Zhang, Q.; Yao, H.; Liang, Z.; Lee, H. W.; Hsu, P. C.; Zheng, G.; Cui, Y. High electrochemical selectivity of edge versus terrace sites in two-dimensional layered MoS_2 materials. *Nano Lett.* **2014**, *14*, 7138−7144.
(20) Fu, Q.; Han, J.; Wang, X.; Xu, P.; Yao, T.; Zhong, J.; Zhong, W.; Liu, S.; Gao, T.; Zhang, Z. 2D transition metal dichalcogenides: Design, modulation, and challenges in electrocatalysis. *Adv. Mater.* **2020**, *33*, No. 1907818.
(21) Laursen, A. B.; Kegnæs, S.; Dahl, S.; Chorkendorff, I. Molybdenum sulfides—efficient and viable materials for electro-and photoelectrocatalytic hydrogen evolution. *Energy. Environ. Sci.* **2012**, *5*, 5577−5591.
(22) Ouyang, Y.; Ling, C.; Chen, Q.; Wang, Z.; Shi, L.; Wang, J. Activating inert basal planes of MoS_2 for hydrogen evolution reaction through the formation of different intrinsic defects. *Chem. Mater.* **2016**, *28*, 4390−4396.
(23) Sarma, P. V.; Tiwary, C. S.; Radhakrishnan, S.; Ajayan, P. M.; Shaijumon, M. M. Oxygen incorporated WS_2 nanoclusters with superior electrocatalytic properties for hydrogen evolution reaction. *Nanoscale* **2018**, *10*, 9516−9524.
(24) Sarma, P. V.; Kayal, A.; Sharma, C. H.; Thalakulam, M.; Mitra, J.; Shaijumon, M. Electrocatalysis on edge-rich spiral WS_2 for hydrogen evolution. *ACS Nano* **2019**, *13*, 10448−10455.
(25) Han, J. H.; Kim, H. K.; Baek, B.; Han, J.; Ahn, H. S.; Baik, M. H.; Cheon, J. Activation of the basal plane in two dimensional transition metal chalcogenide nanostructures. *J. Am. Chem. Soc.* **2018**, *140*, 13663−13671.
(26) Chen, Y.; Ou, P.; Bie, X.; Song, J. Basal plane activation in monolayer $MoTe_2$ for the hydrogen evolution reaction via phase boundaries. *J. Mater. Chem. A* **2020**, *8*, 19522−19532.
(27) Voiry, D.; Salehi, M.; Silva, R.; Fujita, T.; Chen, M.; Asefa, T.; Shenoy, V. B.; Eda, G.; Chhowalla, M. Conducting MoS_2 nanosheets as catalysts for hydrogen evolution reaction. *Nano Lett.* **2013**, *13*, 6222−6227.
(28) Yu, Y.; Nam, G. H.; He, Q.; Wu, X. J.; Zhang, K.; Yang, Z.; Chen, J.; Ma, Q.; Zhao, M.; Liu, Z.; et al. High phase-purity 1T′-MoS_2 and 1T′-$MoSe_2$-layered crystals. *Nat. Chem.* **2018**, *10*, 638−643.
(29) Kappera, R.; Voiry, D.; Yalcin, S. E.; Branch, B.; Gupta, G.; Mohite, A. D.; Chhowalla, M. Phase-engineered low-resistance contacts for ultrathin MoS_2 transistors. *Nat. Mater.* **2014**, *13*, 1128−1134.
(30) Wu, L.; Dzade, N. Y.; Yu, M.; Mezari, B.; van Hoof, A. J.; Friedrich, H.; de Leeuw, N. H.; Hensen, E. J.; Hofmann, J. P. Unraveling the role of Lithium in enhancing the hydrogen evolution activity of MoS_2: intercalation versus adsorption. *ACS Energy Lett.* **2019**, *4*, 1733−1740.
(31) Tan, Y.; Luo, F.; Zhu, M.; Xu, X.; Ye, Y.; Li, B.; Wang, G.; Luo, W.; Zheng, X.; Wu, N.; et al. Controllable 2H-to-1T′ phase transition in few-layer $MoTe_2$. *Nanoscale* **2018**, *10*, 19964−19971.
(32) Cho, S.; Kim, S.; Kim, J. H.; Zhao, J.; Seok, J.; Keum, D. H.; Baik, J.; Choe, D. H.; Chang, K. J.; Suenaga, K.; et al. Phase patterning for ohmic homojunction contact in $MoTe_2$. *Science* **2015**, *349*, 625−628.
(33) Leng, K.; Chen, Z.; Zhao, X.; Tang, W.; Tian, B.; Nai, C. T.; Zhou, W.; Loh, K. P. Phase restructuring in transition metal dichalcogenides for highly stable energy storage. *ACS Nano* **2016**, *10*, 9208−9215.
(34) Duerloo, K. A. N.; Li, Y.; Reed, E. J. Structural phase transitions in two-dimensional Mo-and W-dichalcogenide monolayers. *Nat. Commun.* **2014**, *5*, No. 4214.
(35) Lukowski, M. A.; Daniel, A. S.; Meng, F.; Forticaux, A.; Li, L.; Jin, S. Enhanced hydrogen evolution catalysis from chemically exfoliated metallic MoS_2 nanosheets. *J. Am. Chem. Soc.* **2013**, *135*, 10274−10277.
(36) Tsai, C.; Chan, K.; Abild-Pedersen, F.; Nørskov, J. K. Active edge sites in $MoSe_2$ and WSe_2 catalysts for the hydrogen evolution reaction: a density functional study. *Phys. Chem. Chem. Phys.* **2014**, *16*, 13156−13164.
(37) Gupta, U.; Naidu, B.; Maitra, U.; Singh, A.; Shirodkar, S. N.; Waghmare, U. V.; Rao, C. Characterization of few-layer 1T-$MoSe_2$ and its superior performance in the visible-light induced hydrogen evolution reaction. *APL Mater.* **2014**, *2*, No. 092802.
(38) Wong, H.; Ou, X.; Zhuang, M.; Liu, Z.; Hossain, M. D.; Cai, Y.; Liu, H.; Lee, H.; Wang, C.; Luo, Z. Selenium Edge as Selective Anchoring Site for Lithium-Sulfur Batteries with MoSe2/Graphene-based Cathodes. *ACS Appl. Mater. Interfaces* **2019**, *11*, 19986−19993.
(39) Tian, W.; Xi, B.; Feng, Z.; Li, H.; Feng, J.; Xiong, S. Sulfiphilic Few-Layered $MoSe_2$ Nanoflakes Decorated rGO as a Highly Efficient Sulfur Host for Lithium-Sulfur Batteries. *Adv. Energy. Mater.* **2019**, *9*, No. 1901896.
(40) Meng, L.; Yao, Y.; Liu, J.; Wang, Z.; Qian, D.; Zheng, L.; Su, B. L.; Wang, H. E. $MoSe_2$ nanosheets as a functional host for lithium-sulfur batteries. *J. Energy Chem.* **2020**, *47*, 241−247.
(41) Putungan, D. B.; Lin, S. H.; Kuo, J. L. A first-principles examination of conducting monolayer 1T′-MX_2 (M = Mo, W; X = S, Se, Te): promising catalysts for hydrogen evolution reaction and its enhancement by strain. *Phys. Chem. Chem. Phys.* **2015**, *17*, 21702−21708.
(42) Zhang, Q.; Wang, Y.; Seh, Z. W.; Fu, Z.; Zhang, R.; Cui, Y. Understanding the anchoring effect of two-dimensional layered materials for lithium−sulfur batteries. *Nano Lett.* **2015**, *15*, 3780−3786.
(43) Liu, H.; Chen, B.; Qin, H.; Wang, N.; Liu, E.; Shi, C.; Zhao, N. ReS_2 nanosheets anchored on rGO as an efficient polysulfides immobilizer and electrocatalyst for Li-S batteries. *Appl. Surf. Sci.* **2020**, *505*, No. 144586.
(44) Yin, Y.; Zhang, Y.; Gao, T.; Yao, T.; Zhang, X.; Han, J.; Wang, X.; Zhang, Z.; Xu, P.; Zhang, P.; et al. Synergistic phase and disorder engineering in 1T-$MoSe_2$ nanosheets for enhanced hydrogen-evolution reaction. *Adv. Mater.* **2017**, *29*, No. 1700311.
(45) Haseeb, H. H.; Li, Y.; Ayub, S.; Fang, Q.; Yu, L.; Xu, K.; Ma, F. Defective phosphorene as a promising anchoring material for lithium−sulfur batteries. *J. Phys. Chem. C* **2020**, *124*, 2739−2746.
(46) Masurkar, N.; Thangavel, N. K.; Arava, L. M. R. CVD-Grown $MoSe_2$ Nanoflowers with Dual Active Sites for Efficient Electrochemical Hydrogen Evolution Reaction. *ACS Appl. Mater. Interfaces* **2018**, *10*, 27771−27779.
(47) Tongay, S.; Zhou, J.; Ataca, C.; Lo, K.; Matthews, T. S.; Li, J.; Grossman, J. C.; Wu, J. Thermally driven crossover from indirect toward direct bandgap in 2D semiconductors: $MoSe_2$ versus MoS_2. *Nano Lett.* **2012**, *12*, 5576−5580.
(48) Dai, T. J.; Liu, Y. C.; Fan, X. D.; Liu, X. Z.; Xie, D.; Li, Y. R. Synthesis of few-layer 2H-$MoSe_2$ thin films with wafer-level homogeneity for high-performance photodetector. *Nanophotonics* **2018**, *7*, 1959−1969.
(49) Zhao, Y.; Lee, H.; Choi, W.; Fei, W.; Lee, C. J. Large-area synthesis of monolayer $MoSe_2$ films on SiO_2/Si substrates by

https://doi.org/10.1021/acsami.2c05508
ACS Appl. Mater. Interfaces 2022, 14, 24486−24496

atmospheric pressure chemical vapor deposition. *RSC Adv.* **2017**, *7*, 27969−27973.
(50) Kim, K.; Lee, J. U.; Nam, D.; Cheong, H. Davydov splitting and excitonic resonance effects in Raman spectra of few-layer $MoSe_2$. *ACS Nano* **2016**, *10*, 8113−8120.
(51) Elazari, R.; Salitra, G.; Garsuch, A.; Panchenko, A.; Aurbach, D. Sulfur-impregnated activated carbon fiber cloth as a binder-free cathode for rechargeable Li-S batteries. *Adv. Mater.* **2011**, *23*, 5641−5644.
(52) Miao, L.; Wang, W.; Yuan, K.; Yang, Y.; Wang, A. A lithium−sulfur cathode with high sulfur loading and high capacity per area: a binder-free carbon fiber cloth−sulfur material. *Chem. Commun.* **2014**, *50*, 13231−13234.
(53) Liu, Z.; Zhang, X.; Gong, Y.; Lu, Q.; Zhang, Z.; Cheng, H.; Ma, Q.; Chen, J.; Zhao, M.; Chen, B.; et al. Synthesis of MoX_2 (X = Se or S) monolayers with high-concentration 1T′ phase on 4H/fcc-Au nanorods for hydrogen evolution. *Nano Res.* **2019**, *12*, 1301−1305.
(54) Deng, S.; Zhong, Y.; Zeng, Y.; Wang, Y.; Yao, Z.; Yang, F.; Lin, S.; Wang, X.; Lu, X.; Xia, X.; Tu, J. Directional Construction of Vertical Nitrogen-Doped 1T-2H $MoSe_2$/Graphene Shell/Core Nanoflake Arrays for Efficient Hydrogen Evolution Reaction. *Adv. Mater.* **2017**, *29*, No. 1700748.
(55) Guo, J.; Shi, Y.; Bai, X.; Wang, X.; Ma, T. Atomically thin $MoSe_2$/graphene and WSe_2/graphene nanosheets for the highly efficient oxygen reduction reaction. *J. Mater. Chem. A* **2015**, *3*, 24397−24404.
(56) Wang, W.; Huai, L.; Wu, S.; Shan, J.; Zhu, J.; Liu, Z.; Yue, L.; Li, Y. Ultrahigh-Volumetric-Energy-Density Lithium−Sulfur Batteries with Lean Electrolyte Enabled by Cobalt-Doped $MoSe_2/Ti_3C_2T_x$ MXene Bifunctional Catalyst. *ACS Nano* **2021**, *15*, 11619−11633.
(57) Zu, C.; Fu, Y.; Manthiram, A. Highly reversible Li/dissolved polysulfide batteries with binder-free carbon nanofiber electrodes. *J. Mater. Chem. A* **2013**, *1*, 10362−10367.
(58) Mahankali, K.; Thangavel, N. K.; Reddy Arava, L. M. In Situ Electrochemical Mapping of Lithium−Sulfur Battery Interfaces Using AFM−SECM. *Nano Lett.* **2019**, *19*, 5229−5236.
(59) Rohaizad, N.; Mayorga-Martinez, C. C.; Sofer, Z.; Pumera, M. 1T-Phase Transition Metal Dichalcogenides (MoS_2, $MoSe_2$, WS_2, and WSe_2) with Fast Heterogeneous Electron Transfer: Application on Second-Generation Enzyme-Based Biosensor. *ACS Appl. Mater. Interfaces* **2017**, *9*, 40697−40706.
(60) Lu, Q.; Zou, X.; Ran, R.; Zhou, W.; Liao, K.; Shao, Z. An "electronegative" bifunctional coating layer: simultaneous regulation of polysulfide and Li-ion adsorption sites for long-cycling and "dendrite-free" Li−S batteries. *J. Mater. Chem. A* **2019**, *7*, 22463−22474.
(61) He, M.; Yuan, L. X.; Zhang, W. X.; Hu, X. L.; Huang, Y. H. Enhanced cyclability for sulfur cathode achieved by a water-soluble binder. *J. Phys. Chem. C* **2011**, *115*, 15703−15709.
(62) Mahankali, K.; Thangavel, N. K.; Ding, Y.; Putatunda, S. K.; Arava, L. M. R. Interfacial behavior of water-in-salt electrolytes at porous electrodes and its effect on supercapacitor performance. *Electrochim. Acta* **2019**, *326*, No. 134989.
(63) Deng, Z.; Zhang, Z.; Lai, Y.; Liu, J.; Li, J.; Liu, Y. Electrochemical impedance spectroscopy study of a lithium/sulfur battery: modeling and analysis of capacity fading. *J. Electrochem. Soc.* **2013**, *160*, A553.
(64) Kong, W.; Yan, L.; Luo, Y.; Wang, D.; Jiang, K.; Li, Q.; Fan, S.; Wang, J. Ultrathin MnO_2/graphene oxide/carbon nanotube interlayer as efficient polysulfide-trapping shield for high-performance Li−S batteries. *Adv. Funct. Mater.* **2017**, *27*, No. 1606663.
(65) Zegeye, T. A.; Kuo, C. F. J.; Wotango, A. S.; Pan, C. J.; Chen, H. M.; Haregewoin, A. M.; Cheng, J. H.; Su, W. N.; Hwang, B. J. Hybrid nanostructured microporous carbon-mesoporous carbon doped titanium dioxide/sulfur composite positive electrode materials for rechargeable lithium-sulfur batteries. *J. Power Sources* **2016**, *324*, 239−252.
(66) Hua, W.; Li, H.; Pei, C.; Xia, J.; Sun, Y.; Zhang, C.; Lv, W.; Tao, Y.; Jiao, Y.; Zhang, B.; et al. Selective catalysis remedies polysulfide shuttling in lithium-sulfur batteries. *Adv. Mater.* **2021**, *33*, No. 2101006.
(67) Cao, D.; Shen, T.; Liang, P.; Chen, X.; Shu, H. Role of Chemical Potential in Flake Shape and Edge Properties of Monolayer MoS_2. *J. Phys. Chem. C* **2015**, *119*, 4294−4301.
(68) Shi, Y.; Zhou, W.; Lu, A. Y.; Fang, W.; Lee, Y. H.; Hsu, A. L.; Kim, S. M.; Kim, K. K.; Yang, H. Y.; Li, L. J.; et al. van der Waals epitaxy of MoS_2 layers using graphene as growth templates. *Nano Lett.* **2012**, *12*, 2784−2791.
(69) Huang, J. K.; Pu, J.; Hsu, C. L.; Chiu, M. H.; Juang, Z. Y.; Chang, Y. H.; Chang, W. H.; Iwasa, Y.; Takenobu, T.; Li, L. J. Large-area synthesis of highly crystalline WSe_2 monolayers and device applications. *ACS Nano* **2014**, *8*, 923−930.

https://doi.org/10.1021/acsami.2c05508
ACS Appl. Mater. Interfaces 2022, 14, 24486−24496